CHAPTER 2 – IMPROVED DETECTION OF BOTTOM CRACKS IN WEEP HOLES USING SIGNAL MEASUREMENTS BY A MOVING TRANSDUCER

2.1 Background

Two types of fatigue cracks have been observed emanating from weep holes, top cracks that emanate upward and bottom cracks that propagate toward the wing surface. Figure 2.1 displays a diagram of a weep hole with a bottom crack and an ultrasonic transducer. In [16], separate automated inspection approaches were developed to detect top and bottom cracks. When considering the expected variation in crack size and crack location on the weep hole, conventional C-scan bottom crack inspection requires scanning from both directions along the riser. To reduce inspection time, the goal for the automated bottom crack inspection procedure was to obtain better performance through scanning from a single direction, thus reducing the scan time by one half. To meet this goal, a multilayer algorithm was developed using both C-scan images and A-scan signals. For the final phase of the algorithm, an approach using the A-scan signals was developed to assess the existence of two hill signals versus one hill signal to separate the smaller bottom crack cases from the no crack case. The original approach used a measure of the asymmetry of the A-scan signal after centering the signal using cross correlation with a reference specular signal [23].

During in-field experimentation, this technique was found to produce some false bottom crack calls and was unable to detect certain small bottom crack cases [22]. This work presents an improved approach that uses the variation in the A-scan signals as the transducer is incrementally moved along the wing surface in a region where a bottom crack may exist. The primary advantage of this technique is the ability to detect superimposed signals independently from the general shape of the transient pulse. A comparison of the inspection capability between the refined automated protocol and conventional inspection through viewing C-scan images is presented.

2.2 BEM Model Formulation for Transient Elastodynamic Problems

Transient elastodynamic simulations using the boundary element method (BEM) were developed as an aid to interpret the raw transducer signals. Figure 2.2 displays the model diagram of a cylindrical hole with a notch. Models for both notches and open cracks on the cylindrical hole were formulated. The equation of motion for an elastic solid is given by

$$(\lambda + \mu)\tilde{\nabla}\tilde{\nabla} \cdot \mathbf{u}(\mathbf{x},t) + \mu\nabla^2\mathbf{u}(\mathbf{x},t) = \rho\ddot{\mathbf{u}}(\mathbf{x},t) \tag{2.1}$$

To define the traction conditions, Hooke's law and the strain components are used.

To obtain the transient solution, an approach incorporating a 2D frequency domain boundary element method was used. Fourier transforms using the Fast Fourier Transform (FFT) algorithm were first used to convert the transient problem into a series

of frequency domain problems. The steady state form of the equation of motion in the transformed domain for an elastic solid is given by

$$(l+m)\tilde{\mathbf{N}}\tilde{\mathbf{N}}\cdot\hat{\mathbf{u}}(\mathbf{x},w)+m\nabla^2\hat{\mathbf{u}}(\mathbf{x},w)+rw^2\hat{\mathbf{u}}(\mathbf{x},w)=0 \tag{2.2}$$

For the problem shown in Figure 2.2, a traction free boundary exists, where

$$\hat{t}_n(\mathbf{x},w)=0,\ x\in\partial V, \tag{2.3}$$

$$\hat{t}_t(\mathbf{x},w)=0,\ x\in\partial V. \tag{2.4}$$

Now consider an arbitrary incident displacement field, $\mathbf{u^i}$, in the elastic medium. The field scattered from the boundary will be defined as $\mathbf{u^{sc}}$. Thus the superposition of these two fields gives the total field response in the elastic medium, $\mathbf{u^t}$. By substituting the corresponding tractions, $\mathbf{t^i}$ + $\mathbf{t^{sc}}$ for $\mathbf{t^t}$, the boundary conditions become,

$$\hat{t}_n^{\,sc}(\mathbf{x},w)=-\hat{t}_n^{\,i}(\mathbf{x},w),\ x\in\partial V, \tag{2.5}$$

$$\hat{t}_t^{\,sc}(\mathbf{x},w)=-\hat{t}_t^{\,i}(\mathbf{x},w),\ x\in\partial V. \tag{2.6}$$

An integral representation of the elastic media can be defined as shown in [24]. The integral equation for an infinite elastic domain can be represented by

$$\int_{\partial V}\left[\mathbf{U}(\mathbf{x},y;w)\hat{\mathbf{t}}^{sc}(y,w)-\mathbf{T}(\mathbf{x},y;w)\hat{\mathbf{u}}^{sc}(y,w)\right]\mathrm{dS}_y=\begin{cases}\hat{\mathbf{u}}^{sc}(\mathbf{x},w), & \mathbf{x}\in \mathrm{V}\\ 0, & \mathbf{x}\notin \mathrm{V}\end{cases}. \tag{2.7}$$

The fundamental solution for the two dimensional problem, **U,** and the double layer kernal, **T,** are given respectively by

$$\mathbf{U}(\mathbf{x},y)=\frac{i}{4m}\left[H_0^{(1)}(k_Tr)+\frac{1}{(k_T)^2}\nabla\nabla\left(H_0^{(1)}(k_Tr)-H_0^{(1)}(k_Lr)\right)\right], \tag{2.8}$$

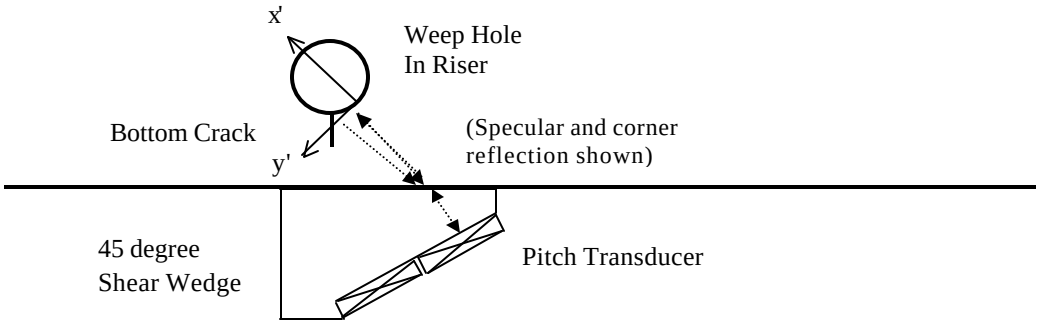

Figure 2.1. Diagram of a weep hole with a bottom crack and transducer acting in pulse-echo mode.

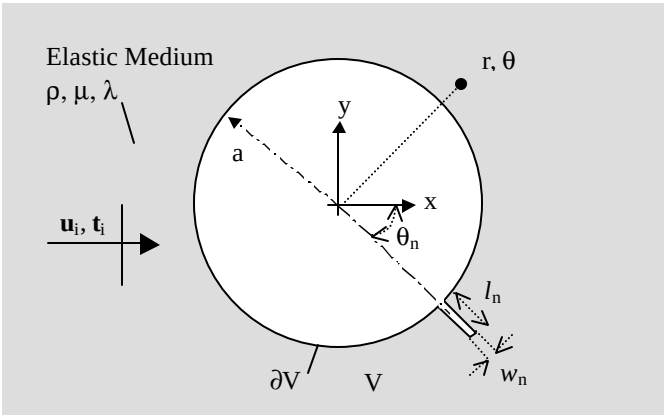

Figure 2.2. Cylindrical hole with a notch in an infinite elastic medium.

$$\mathbf{T}(\mathbf{x}, y) = \overset{n}{\mathbf{T}}(\, l, m, \partial_y)\mathbf{U}(\mathbf{x}, y)\,, \tag{2.9}$$

which can be found in the reference by Niwa et al. [25]. At this point, the boundaries are discretized into elements, and a system of equations is derived to represent the integral equation. The details by which the matrix equation is derived can be found in the literature [26-28]. Following substitution of the boundary conditions, the result can be represented by the following matrix equation for an elastic solid,

$$\mathbf{H}^{(1)}\hat{\mathbf{u}}^{sc} = -\mathbf{G}^{(1)}\hat{\mathbf{t}}^{i}\,, \tag{2.10}$$

where $\mathbf{H}^{(1)}$ and $\mathbf{G}^{(1)}$ are matrices resulting from the numerical integration of the displacement and traction components of the integral equation respectively about the discretized domain. Upon solution of the series of frequency domain problems, the inverse Fourier Transform was subsequently used to assemble the transient solution for the scattered field problem at the boundary and at any internal points of interest. To obtain the total field response, the scattered and free field responses were summed.

Several modeling strategies were used to minimize computational time while preserving the accuracy of the calculations. First, a single domain boundary was defined for the cylindrical hole with an open crack or notch. To eliminate error due to the close proximity of the boundary element nodes, a finite width for the notch and crack was used. To approximate the singular nature of the field near the tip of a fatigue crack, the tip of the notch was modeled using a quarter-point element. Second, to eliminate the computational time required for the solution of the incident transducer field using the BEM method, a gaussian beam representation of the transducer response was used. Also,

comparable locations for the transducers within the infinite elastic medium were used. Through these approximations, considerable computational time was saved while good agreement with experimental data was found. Appendix A presents additional details concerning the boundary element formulation and the simulation parameter settings.

Under certain test conditions, limitations exist in the inspection of weep holes using only C-scan data. Challenging conditions include smaller bottom cracks (~0.020 in.) and bottom cracks that are skewed from the normal direction (with respect to the wing surface). These cases were further examined using the 2D boundary element method (BEM) simulation of an incident transient pulse on a weep hole. Figures 2.3-5 display contour plots of the total displacement field generated by an incident in-plane shear pulse on a weep hole for the conditions of no bottom notch, and for the cases of a 0.070" bottom notch (normal to wing surface) and a 0.018" bottom notch skewed 10° in the CCW direction respectively. The six snapshots in time represent $\tau = 0,1,2,3,4,5$ where τ is defined by $\tau = 2*(t-t_o)*c_t/r$. Here, c_t is the shear wave speed of the material, r is the radius of the weep hole and t_o is a reference time. The simulations were generated for the following parameters: diameter of weep hole = 0.250", material properties of aluminum, in-plane shear pulse generated by a 0.250" transducer with a center frequency of 3.7 MHz, center of pitch transducer at (−0.640",0.085") in the x'y'coordinate system (shown in Figure 2.1.) Additional details for the simulation are presented in Appendix A.

For the no bottom notch case (Figure 2.3), only specular reflection from the weep hole travels back toward the pitch transducer (in the negative x' direction). For the

0.070” notch case (Figure 2.4), a significant second signal due to the corner reflection between the notch and the weep hole is observed following the specular signal from the weep hole. When considering the case of a smaller notch with some skew in location in the counter clockwise (CCW) direction (Figure 2.5), this second signal is both reduced and superimposed on the specular weep hole signal. Although significant differences in the transient signal exist with respect to the no crack case, traditional C-scan approaches are unable to detect such flaw cases.

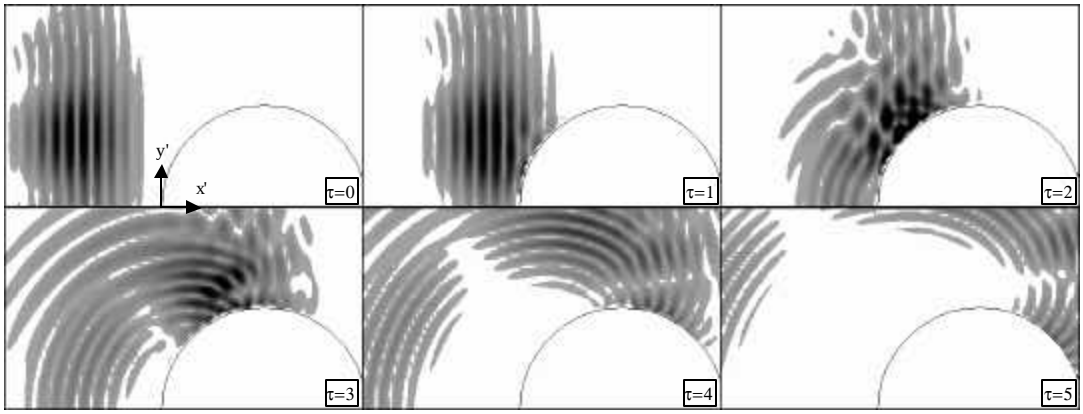

Figure 2.3. Contour plot of response to incident shear pulse – no crack case.

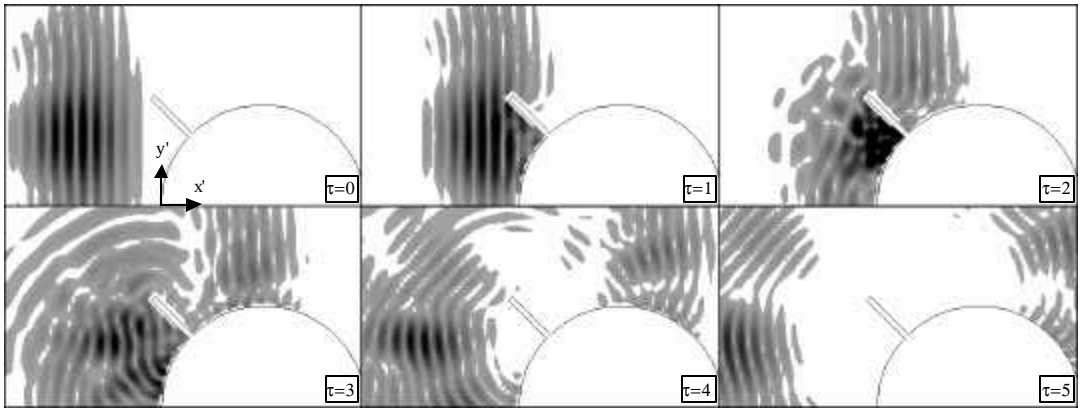

Figure 2.4. Contour plot of response to incident shear pulse – with 0.070" bottom crack.

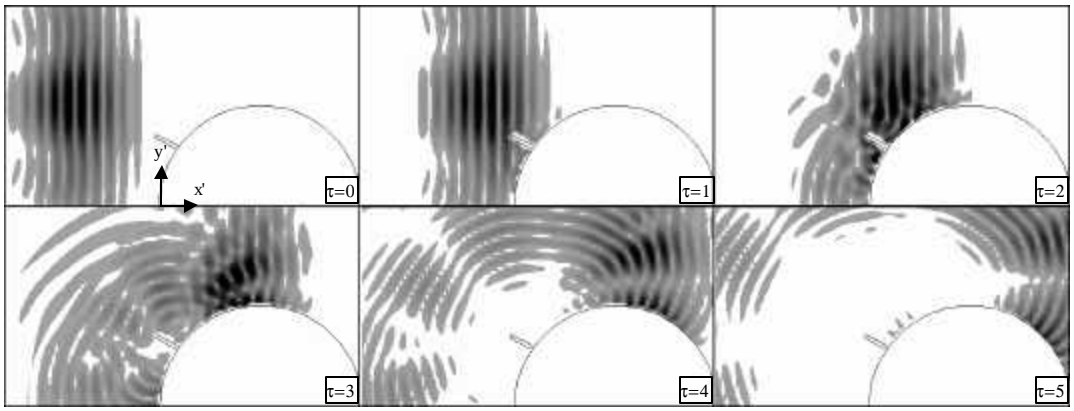

Figure 2.5. Contour plot of response to incident shear pulse – with 0.018" bottom crack skewed 10° CCW.

2.3 Preliminary Bottom Crack Detection Algorithm

Figure 2.1 displays a weep hole with a bottom crack and an ultrasonic transducer. Details concerning the ultrasonic inspection system used in conjunction with this approach have been previously presented [23]. For bottom crack detection, a shear signal is generated into the riser and pulse-echo inspection is performed. A C-scan amplitude plot is acquired and used to determine the presence of a typical bottom crack. For a typical bottom crack case, the amplitude plot contains two peaks due to the specular reflection from a weep hole and the corner reflection between the hole and the crack. An approach incorporating three sub-neural networks was developed to detect two peaks in the amplitude plot, which would indicate the presence of a bottom crack. An earlier paper describes this procedure in greater detail [22]. The schematic for this procedure is show in Figure 2.6. The function of this algorithm is identical to the function performed by inspectors viewing the same C-scan images and assessing the existence of one or two peaks for each weep hole detected.

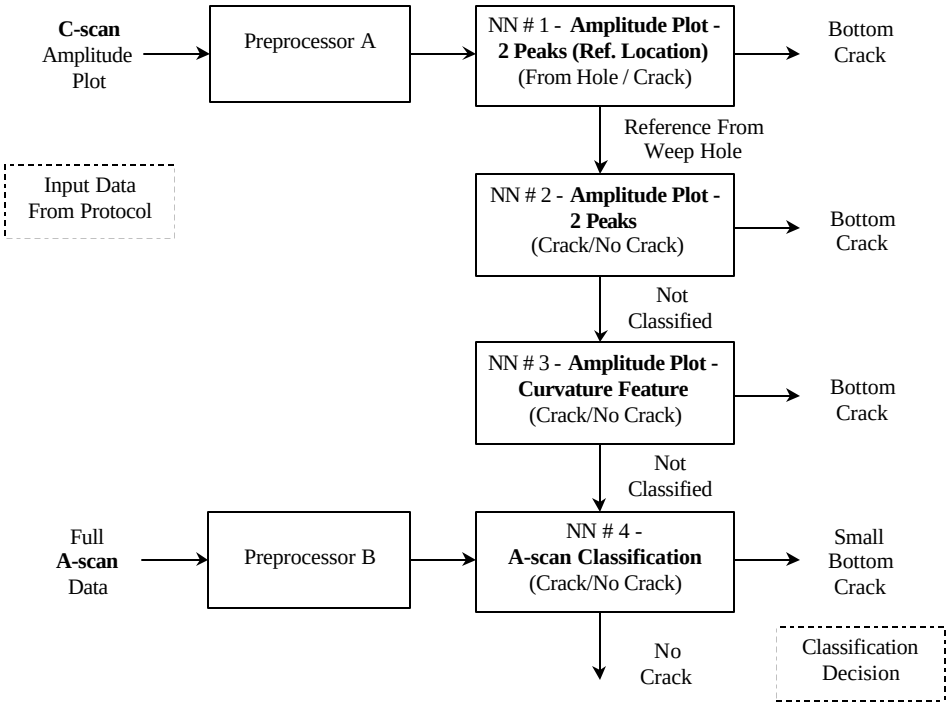

Figure 2.6. Schematic flow chart for bottom crack detection procedure

Additional information in the A-scan of the specular reflection was employed for improving the bottom crack detection capability of the procedure. Figure 2.7 displays weep hole specular reflection signals centered with the specular reference using cross correlation for (a) the no bottom crack case and (b) the bottom crack case. Although the signal reflected from the corner of the crack is superimposed on the specularly reflected signal from the hole, the two peaks in the signal can be used to separate the presence of a smaller bottom crack from the no crack case. A fourth layer to classify this A-scan data has been included in the procedure (Figure 2.6).

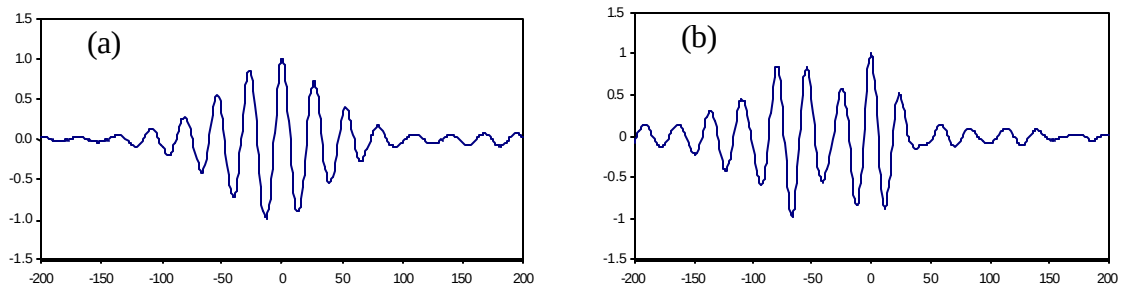

Figure 2.7. Centered reflection signals from a weep hole (a) with no bottom crack and (b) with a bottom crack. (plot contains normalized time step along x-axis).

2.4 Multiple Signal Classification

One of the major challenges in ultrasonic flaw detection is to classify multiple signals within a single scan. Conditions often exist where flaws are located near geometrical features such as cylindrical holes that also produce significant ultrasonic signals. These cases generate multiple ultrasonic signals which are often closely spaced or sometimes superimposed such as in Figure 2.7(b). This lack of separation may be found both in the time domain (in terms of A-scan data) and in the spatial domain (in terms of C-scan data). Random signals due to grain noise or unusual geometric reflections can add further difficulty to the detection of closely spaced multiple signals of interest.

Several techniques have been reviewed for the possible detection and classification of multiple signals. Table 2.1 separates these techniques into four

categories representing steps in the classification procedure: data enhancement, domain transformation, feature mapping and extraction, and feature classification. Data enhancement is often used to reduce electronic noise and material grain signals. Data enhancement approaches include standard techniques such as time and spatial averaging and filtering [29], and advanced approaches such as the synthetic aperture focussing technique [30,31] and split-spectrum processing [32]. Domain transformations have been applied for the separation of multiple signals. Rectification using the Hilbert transform has been shown to aid in the separation of superimposed time domain signals [33]. Fourier and wavelet transforms have been applied to both 1D and 2D data sets to aid in distinguishing the frequency and spatially varying components of signals [34,35]. The feature mapping and extraction step can be applied to a domain in order to extract characteristics that are of interest. For ultrasonic inspection, these characteristics are dependent upon characteristics of the flaw, and the material and geometric properties of the test sample. Feature mapping often uses multiple data measures (amplitude, phase, time of flight, statistical measures) on the input domain (typically a combination of time, frequency, and spatial domains) to obtained the greatest amount of information about a scan domain [29]. Other feature extraction approaches which have been applied to the classification of multiple signals include correlation techniques, eigenvalues of the covariance matrix of the feature vector [36], and the fitting of gaussian mixtures [37]. Feature classification is typically applied in the final step using such tools as threshold comparison, expert systems, fuzzy logic and neural networks. Typically, combinations of these approaches are used to optimize data analysis and classification [29].

Table 2.1. Review of multiple signal classification approaches.

Data Enhancement	■ Time Averaging and Filtering ■ Spatial Averaging and Filtering ■ Synthetic Aperture Focusing Technique ■ Split Spectrum Processing
Domain Transformation	■ Rectification of Time Signal (Hilbert Transform) ■ Frequency Domain (Fourier Transform) ■ Wavelet Transform ■ Transfer Function through Deconvolution

Feature Mapping / Extraction	■ Correlation (cross correlation w/reference)
	■ Eigenvalues of Covariance Matrix
	■ Fitting Guassian Mixtures
	■ Time/Frequency Domain Feature Mapping
	  ■ Amplitude / Energy / Width of pulse
	  ■ Standard Deviation / Skewness / Kurtosis of peak
	■ Clustering Algorithms - 2D/3D Feature Extraction

Feature Classification	■ Threshold Comparison ■ Rule Based Approach / Expert System ■ Fuzzy Logic ■ Neural Networks

In this work, first a procedure measuring the asymmetry of the signal was implemented to detect a small bottom crack signal in the specular signal from the weep hole. After centering the A-scan signal using cross-correlation with the specular reference signal, a calculation of the skewness of the centered signal is performed. This procedure is repeated at 20 locations (4 by 5 scan step grid) and the results are entered into a neural network for classification. The preliminary validation results following training are shown in Table 2.2. The procedure was found to be quite successful in separating typical cases such as the no bottom crack case shown in Figure 2.7(a) and the bottom crack case shown in Figure 2.7(b). However, one missed bottom crack and four false call cases were of concern. Figure 2.8(a) plots the A-scan response for a false call due to asymmetry in the signal produced by an unpainted wing surface and a square pulser. Figure 2.8(b) shows a missed crack case where the corner reflected signal from

the bottom crack produces no significant second pulse. Alternative multiple signal classification approaches presented in Table 2.1 were explored but were unable to aid in the proper classification of these irregular signals.

Table 2.2. Validation results of automated classification scheme for 208 weep hole cases (72 bottom crack cases, 70 with top crack cases).

	Number of **No Crack Calls**	Number of **False Calls for No Crack Cases**	Number of **Cracks Detected**	Number of **Missed Cracks**
Bottom Crack NN #1-3 (C-scan)	-	0	63	-
Bottom Crack NN #4 (A-scan)	130	6	8	1
Bottom Crack Results	**130**	**6**	**71**	**1**

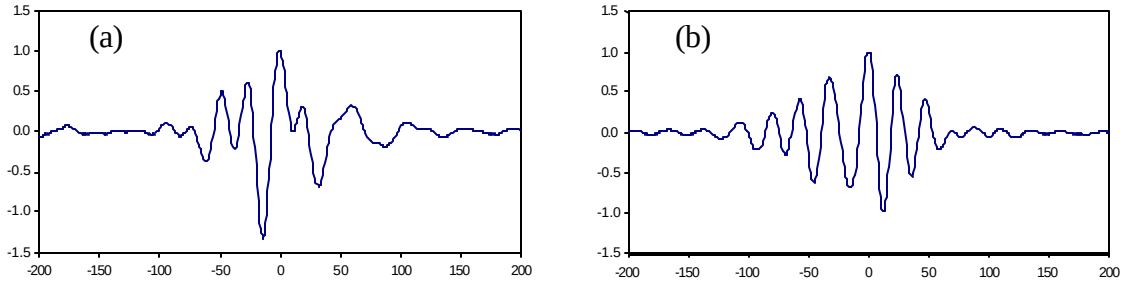

Figure 2.8. Centered reflection signals from a weep hole (c) no crack case with an unpainted panel surface and a square pulser, (d) with small bottom crack (plot contains normalized time step along x-axis).

2.5 Proposed Procedure Using Spatial Signal Variation

The objective of a refined bottom crack detection algorithm using the A-scan data is that it must be insensitive to the A-scan pulse shape characteristics. To overcome the effect of the pulse shape, it was observed that as a transducer is moved in the pulse-echo mode across a weep hole near the bottom crack region, changes exist in the relative amplitude as do small changes in the time of flight between the specular reflection and the corner reflection from a crack. Since the shape of specular signals from the weep hole vary little between transducer positions in this area, any significant change in the shape of the pulse must thus be produced by the existence of a bottom crack. Recent work has discussed the use of monitoring the change of A-scan signals in the frequency domain for the detection of surface breaking cracks using a laser ultrasonic source [38]. Other B-scan analysis approaches have been proposed [39,40]. In the present work, an alternative to the prior approaches was proposed through measurement of the spatial signal variation (SSV) in the time domain. A diagram of this approach is shown in Figure 2.9. The standard deviation between the four signals at 401 time locations centered about a reference (to be determined by cross correlation with a reference signal) are calculated and averaged to produce a single measure, μ_S, used for comparison. The equation for the spatial signal variation measure is given by:

$$m_s = \frac{\sum_{i=-m}^{m} \sqrt{\frac{n\sum_{j=1}^{n} x_j(i)^2 - \left(\sum_{j=1}^{n} x_j(i)\right)^2}{n(n-1)}}}{2m+1}, \qquad (2.11)$$

where n, the number of adjacent signals compared, was set to 4 and m is set to 200 (thus averaging a total of 401 time step locations). The transducer step size between each of the four signals is 0.020" beginning at a location 0.120" from the specular reference. Figure 2.10 displays this procedure and the calculated SSV measure, μ_S, for the four cases previously discussed: (a) no bottom crack, (b) with bottom crack, (c) no crack case with an unpainted panel surface and a square pulser, (d) with small bottom crack. By considering the variations between the four chosen signals, all four of these cases were correctly classified. Although the signals in Figure 2.10(c) are irregular, they are consistently irregular as the transducer position is varied and thus do not have a secondary crack signal interfering with the main specular response. Although the signals in Figure 2.10(d) do not display a strong second signal, they do exhibit considerable variation as the transducer position is varied and thus indicate the existence of bottom crack.

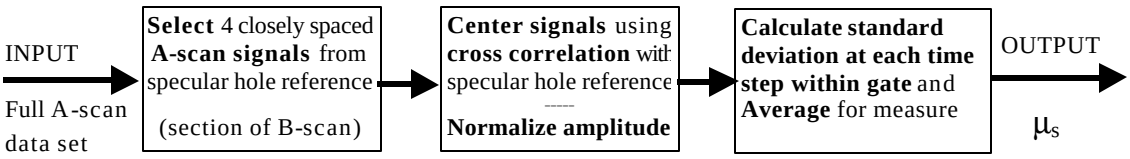

Figure 2.9. Schematic diagram of spatial signal variation approach for refined bottom crack detection.

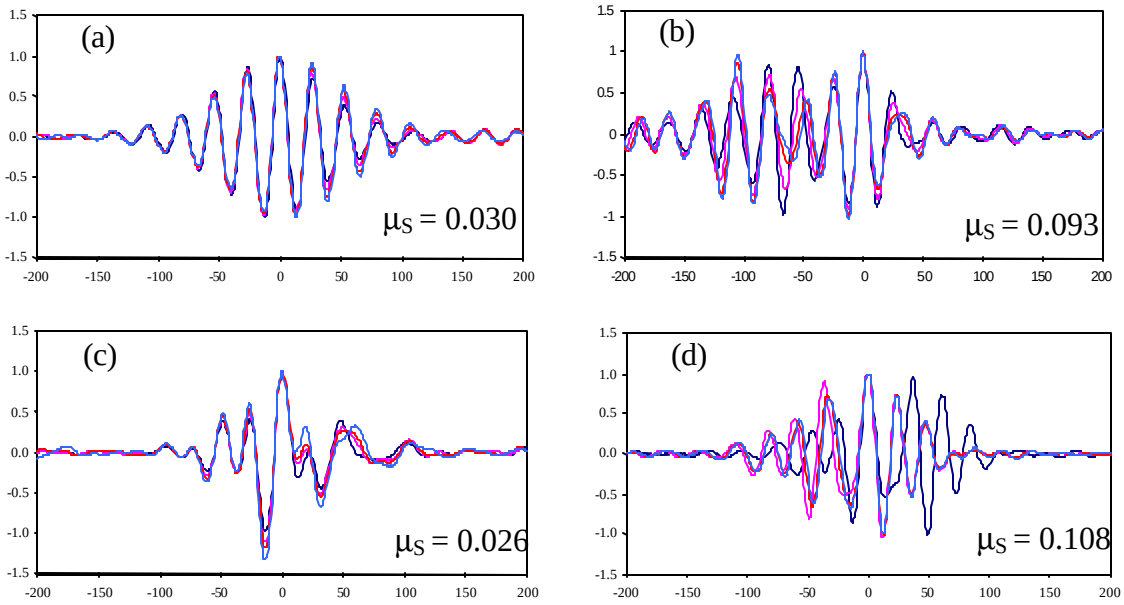

Figure 2.10. Diagram of 4 centered reflection signals displaying the spatial signal variation procedure for four cases (a) no bottom crack, (b) with bottom, (c) no crack case with an unpainted panel surface and a square pulser, (d) with small bottom crack (normalized time step along x-axis).

2.6 Validation of Approach

The refined procedure using spatial signal variation was initially validated with the experimental training set. Table 2.3 displays a summary of the classification results of the training set data. When this approach was used in place of the asymmetry-based procedure, all 72 bottom cracks were detected (versus 71 for the asymmetry procedure from Ref. [23]) and only 2 false calls out of 136 were made (versus 6 false calls for the asymmetry procedure). The two false calls were caused by chatter marks on the weep hole surface, which is not of great concern.

An independent validation of the automated procedure with respect to a C-scan based approach was also performed. The details of this validation have been previously presented [22] and are further discussed in Chapter 3. Table 2.4 displays the comparison of results for the two approaches. In general, the automated procedure significantly improved the detectability of bottom cracks versus the C-scan approach without increasing the false call rate.

The primary advantage of the SSV approach is its ability to detect superimposed signals independently from the general shape of the transient pulse. The automated approach was found to provide a significant improvement in detectability from a single scan direction over the C-scan approach, which requires scanning from both directions. A reduction in scan time by one half as provided by the SSV approach should lead to a significant reduction in inspection costs to the Air Force.

It has been shown in this Chapter that refined detection of cracks using the application of the spatial signal variation approach in a more general form shows considerable promise for practical application. Further work should be carried out to transform this technique into a general feature mapping approach.

Table 2.3. Validation results of improved automated classification scheme for same training set

	Number of **No Crack Calls**	Number of **False Calls for No Crack Cases**	Number of **Cracks Detected**	Number of **Missed Cracks**
Bottom Crack NN #1-3 (C-scan)	-	0	63	-
Bottom Crack NN #4 (A-scan)	134	2	9	0
Bottom Crack Results	**134**	**2**	**72**	**0**

Table 2.4. Summary of PoD validation results for bottom crack detection.

	C-scan Approach	**Automated Classification Approach**
PoD (90%)	**0.024”**	**0.010”**
False Call Rate	**1.6%**	**1.1%**